AGU PUBLICATIONS

JGR

Journal of Geophysical Research: Oceans

RESEARCH ARTICLE

10.1002/2013JC009572

Key Points:
- Irradiance depth profiles can be decomposed using wavelet method
- Light field statistics can be quantified using irradiance depth profiles
- Depth change of irradiance statistics can be derived from its depth profiles

Correspondence to:
J. Wei,
jianwei.wei@umb.edu

Citation:
Wei, J., M. R. Lewis, R. Van Dommelen, C. J. Zappa, and M. S. Twardowski (2014), Wave-induced light field fluctuations in measured irradiance depth profiles: A wavelet analysis, *J. Geophys. Res. Oceans*, *119*, 1344–1364, doi:10.1002/2013JC009572.

Received 1 NOV 2013
Accepted 4 FEB 2014
Accepted article online 11 FEB 2014
Published online 24 FEB 2014

Wave-induced light field fluctuations in measured irradiance depth profiles: A wavelet analysis

Jianwei Wei[1,2], Marlon R. Lewis[2], Ronnie Van Dommelen[3], Christopher J. Zappa[4], and Michael S. Twardowski[5]

[1]School for the Environment, University of Massachusetts Boston, Boston, Massachusetts, USA, [2]Department of Oceanography, Dalhousie University, Halifax, Nova Scotia, Canada, [3]Satlantic LP, Halifax, Nova Scotia, Canada, [4]Lamont-Doherty Earth Observatory, Columbia University, Palisades, New York, USA, [5]Department of Research, WET Labs, Inc., Narragansett, Rhode Island, USA

Abstract Rapid variations in the intensities of light are commonly observed in profiles of downwelling plane irradiance in the ocean. These fluctuations are often treated as noise and filtered out. Here an effort is made to extract the pertinent statistics to quantify the light field fluctuations from vertical profiles of irradiance measured under clear skies. The irradiance data are collected in oceanic and coastal waters using a traditional free-fall downwelling plane irradiance sensor. The irradiance profiles are transformed into time-frequency domain with a wavelet technique. Two signatures including the dominant frequency (<3.5 Hz) and the coefficient of variation of irradiance fluctuations along the water column are identified from the variance spectrum. Both the dominant frequency and the amplitude decrease as the inverse square root of depth, consistent with simple models of wave focusing and data from other studies. Mechanisms contributing to the observed variations and the observational uncertainties are discussed.

1. Introduction

The downwelling plane irradiance (E_d, unit: μWcm^{-2} nm^{-1}) is a key radiometric quantity in hydrologic optics-related applications, and the characteristics of the mean irradiance profile are well documented [*Gordon*, 1989; *Jerlov*, 1976; *Kirk*, 1994; *Preisendorfer*, 1976; *Zaneveld and Spinrad*, 1980]. In the upper water column, the mean irradiance profile is the best fit to an exponential relationship assuming a level surface and a plane-parallel environment with no change in surface illumination over the measurement interval,

$$E_d(z) = E_d(0^-)\exp\left[-\int_0^z K_d(z')dz'\right] \quad (1)$$

where E_d at depth z (unit: m; positive downward) is related to the irradiance just below the sea surface ($E_d(0^-)$) by the diffuse attenuation coefficient K_d(z) (unit: m^{-1}). Variability in the diffuse attenuation coefficient relates directly to key biogeochemical properties of the upper ocean [*Morel and Maritorena*, 2001; *Xing et al.*, 2011].

The irradiance field in the near-surface water column is subject to fluctuations about the mean at varying time scales. Celestial motions cause hourly, daily, seasonal, and yearly changes in the incident irradiance and the subsequent irradiance underwater. These relatively long-term irradiance variations can be predicted to first order [*Gregg and Carder*, 1990; *Sathyendranath and Platt*, 1988]. In the presence of sea-surface waves however, the light refraction occurring at the fluctuating air-sea interface leads to a rapidly changing underwater light field. The wave-induced irradiance fluctuations are readily observable at time scales of a few tens of milliseconds to several seconds [*Darecki et al.*, 2011; *Dera and Gordon*, 1968; *Dera and Stramski*, 1986; *Snyder and Dera*, 1970; *Stramski and Dera*, 1988; *Zaneveld et al.*, 2001]. The vertical distribution of the light fluctuations in the upper water column, including the amplitudes, periods and spectral content, is of ecological significance. In general, and for the open ocean, over half of the integrated primary production takes place in the first 40 m of the water [*Siegel et al.*, 1995] and the rapidly fluctuating light can potentially impact the growth rate, photosynthetic efficiency, or chlorophyll pigmentation for certain species of planktonic algae [*Greene and Gerard*, 1990; *Quéguiner and Legendre*, 1986; *Stramski et al.*, 1993; *Walsh and Legendre*, 1983]. It may strongly influence endosymbiotic photosynthesis of corals inhabiting shallow reef habitats [*Nakamura and Yamasaki*, 2008]. For fish in the littoral zone, their early life stages (comprising eggs, larvae,

and juveniles) respond to the varying light climate [*Stoll*, 2009]. Marine animals' vision is also sensitive to the spatial and temporal fluctuations of the light field [*McFarland and Loew*, 1983]. From a purely physical perspective, the fluctuating irradiance signals are related to, and theoretically could be used to infer, the characteristics of sea-surface wave field.

Determination of the statistical nature of the short-term fluctuations in the irradiance field relies on appropriate sampling strategies. For example, field data in support of understanding the nature of the fluctuating underwater irradiance has been largely acquired with sensors fixed at a nominal depth in the ocean [*Dera and Gordon*, 1968; *Dera et al*., 1993; *Gernez and Antoine*, 2009; *Gernez et al*., 2011; *Gordon et al*., 1971; *Hofmann et al*., 2008; *Nikolayev et al*., 1972; *Nikolayev and Yakubenko*, 1978; *Prokopov et al*., 1975; *Stramska and Dickey*, 1998; *Stramski*, 1986b; *Stramski and Dera*, 1988]. Such observations provide much information on the light field statistics at specific depths. A clearer picture of light field statistics, particularly on the dependency of the magnitude and frequency of irradiance fluctuations on the environmental conditions (solar zenith, wind speed, sky cloudiness, water turbidity, etc.) developed from these methods [*Walker*, 1994, and references therein]. Theoretical investigation often starts with a simplified sea-surface model [*Hieronymi et al*., 2012; *Nikolayev and Khulapov*, 1976; *Schenck*, 1957; *Snyder and Dera*, 1970; *Zaneveld et al*., 2001]; more advanced models reconstruct the sea surface based on existing wave spectra [*McLean and Freeman*, 1996]. Apart from the simplification and some lack of realism, theoretical models play an important role in interpretations of the irradiance fluctuations, and sometimes produce predictions that are consistent with field observations [*You et al*., 2010]. The present knowledge of the statistics of the underwater light field is however limited, inasmuch as the dynamic light field varies in the temporal domain as well as the spatial domain and because of the operational difficulty in measuring the fluctuating field—near the sea surface in particular, but more generally throughout the vertical. For example, the depth evolution of the irradiance fluctuations has been described based on time series measurements at only a few fixed depths in the upper ocean [*Darecki et al*., 2011; *Gernez and Antoine*, 2009; *Snyder and Dera*, 1970].

In this study, an effort is particularly devoted to quantifying the magnitude and frequency structure of the irradiance fluctuations as a function of water depth under clear skies. Different than previous studies, the irradiance depth profiles measured by a free-fall radiometer in the upper ocean water are analyzed. Note that it has long been reported that the irradiance depth profiles are subject to the wave disturbance [e.g., *Zaneveld et al*., 2001; *Zibordi et al*., 2004], but never been treated as useful information. Rather, in optical oceanography practice, such fluctuations are usually filtered out as "noise" from the irradiance depth profiles, to estimate the diffuse attenuation coefficient as under a plane sea surface [*Mueller*, 2003] or multiple casts are carried out and the resultant data statistically averaged [*Zibordi et al*., 2004; *Voss et al*., 2010]. In the current study, the irradiance depth profiles are decomposed with the wavelet transform method (see details in section 3). It is shown that the vertical profiles of irradiance may be used to quantify the dynamic irradiance field for the upper water column such as observed from optical time series taken from sensors lowered from vessels at sea or at fixed positions such as buoys. Furthermore, the methodology allows for a characterization of the dynamic irradiance field induced by sea-surface waves for the upper water column in both the spatial and temporal domain. The vertical resolution could be as high as half meters.

The irradiance depth profiles presented here are representative of sea environments with presence of relatively large surface gravity waves. Hence, we only deal with the irradiance fluctuations varying at relatively slow frequencies ($<$3.5 Hz) and do not resolve the fastest light flashes [e.g., *Stramski and Dera*, 1988].

2. Theoretical Formulation for Wave Focusing

We start with a theoretical examination of the irradiance distribution under a wavy sea surface in the context of geometrical optics. We assume only the direct radiation from the Sun with zenith angle θ_s. The sea surface is modeled as a one-dimensional sine wave,

$$\zeta = \frac{H}{2} \cdot \sin(kx - \omega t) \tag{2}$$

where the surface elevation, ζ (m), is defined in terms of the sea wave height, H (m), the wavenumber, k (rad m^{-1}), the horizontal position, x (m), the angular frequency, ω (rad s^{-1}), and time, t (s). For gravity waves

(wavelength, $\Lambda > 1.73$ cm), the wavenumber k relates to the angular frequency according to the wave dispersion equation in deep waters [*Young*, 1999]

$$f = \frac{\omega}{2\pi} = \frac{\sqrt{gk}}{2\pi} = \sqrt{\frac{g}{2\pi\Lambda}} \tag{3}$$

where Λ (m) is the wavelength, f is the temporal frequency (Hz or s^{-1}), and g is the gravitational acceleration (m s^{-2}). The water below the sea surface is initially assumed purely transparent to light, i.e., no absorption and scattering, and is infinitely deep. At time $t = 0$, there is direct illumination incident onto the sea surface, with solar zenith angle $\theta_s = 0°$. Snell's law is followed at the interface where the rays are refracted. As shown in Figure 1, the waves act as optical lenses, and bundles of light rays are converged to a visual focal point under wave crests and are diverged beneath wave troughs [also see *Minnaert*, 1954; *Schenck*, 1957; *Walker*, 1994; *Zaneveld et al*., 2001]. This wave focusing effect is a consequence of the lensing based on the sea-surface curvature, which is related to both the shape and dimension of surface waves.

The focal depth is defined as the vertical distance from the point of principal intersection to the mean level sea surface. In Figure 2, the focal point O is formed by refracted rays at position A and B, onto which the direct rays are incident from a zenith angle. Assuming the sea surface takes a form of equation (2), the focal depth can be represented as

$$z_f = \Lambda\left[\frac{1}{4}\cos\theta_2 + \frac{H}{2\Lambda}\sin\theta_2\right] \cdot \frac{\sin(\alpha+\theta_3)}{\cos(\alpha+\theta_3+\theta_2)} \tag{4}$$

where θ_2 and θ_3 are the angles of refraction occurring at the wave crest and the inflection point; the other parameters are described as follows:

$$\alpha = \text{atan}\left(\frac{2}{Hk}\right) \tag{5}$$

$$\theta_2 = \text{asin}\left(\sin\theta_s / n_w\right) \tag{6}$$

$$\theta_3 = \text{asin}\left[\frac{\cos(\alpha+\theta_s)}{n_w}\right] \tag{7}$$

In equations (6) and (7), θ_s is the solar zenith angle (in radians) and n_w the dimensionless refractive index of sea water. We derived the above equations independently; similar formulations are also given elsewhere [*McLean and Freeman*, 1996; *Nikolayev et al*., 1972; *Zaneveld et al*., 2001]. In Figure 3a, the focal depth z_f is illustrated as a function of the solar zenith angle and the sea wave steepness, $Hk/2$. This model indicates that the focal depth monotonically decreases with increasing wave slope. In contrast, the focal depth increases until $\theta_s = 25°$ when the sea slopes are large and then decreases with θ_s. Some previous work also estimated this parameter but focused on vertical incidence [e.g., *McLean and Freeman*, 1996; *Zaneveld et al*., 2001].

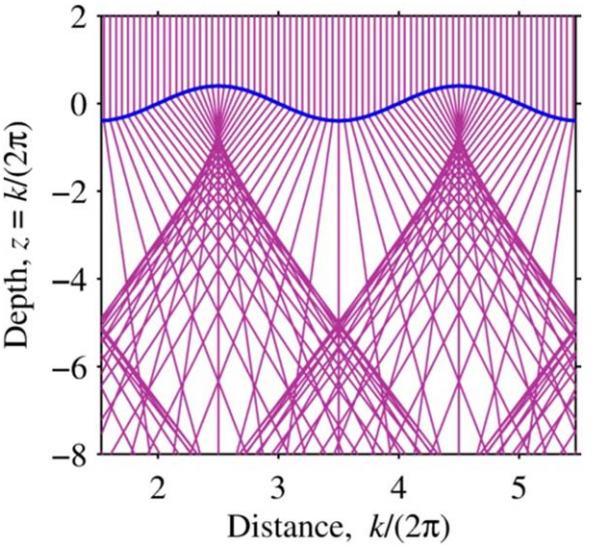

Figure 1. Light geometry under a sine wave (denoted in blue). The incident light is normal to the mean sea surface, represented by a sine wave, $\zeta = 0.4 \times \sin(2\pi x/2)$.

Since the oceanic wave steepness $Hk/2$ is usually less than a threshold value of 0.44–0.55 [*Toffoli et al*., 2010], the ratio of $H/2\Lambda$ is very small (0.070–0.088) and the second term in equation (4) can be safely dropped. Then, by replacing the wavelength term in equation (4) with the dispersion relation in

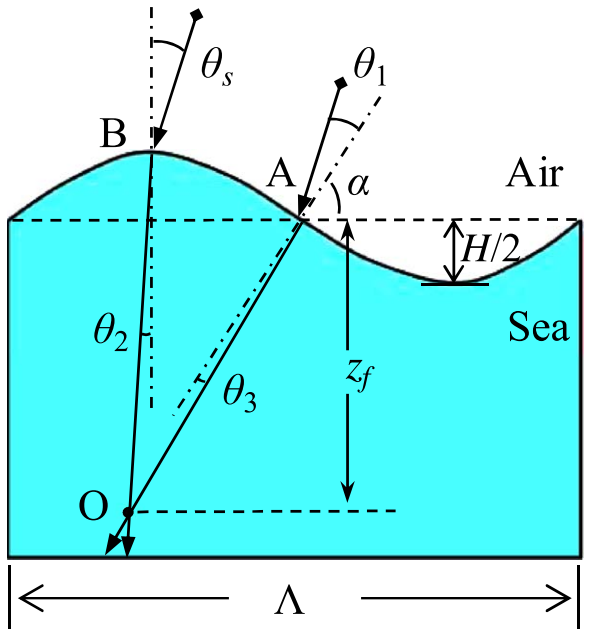

Figure 2. Schematic of focal point of refracted rays under wavy surface. The water body is denoted in cyan.

equation (3), we will have the following power-law function

$$f = F(\theta_s, H, \Lambda) \cdot z_f^{-1/2} \tag{8}$$

where the factor $F(\theta_s, H, \Lambda)$ (unit: $m^{1/2}\ s^{-1}$) is determined by the trigonometric functions of the solar zenith angle and the wave height and length,

$$F = \left[\frac{g\cos\theta_2 \sin(\alpha+\theta_3)}{8\pi\cos(\alpha+\theta_3+\theta_2)}\right]^{1/2} \tag{9}$$

The subscript "*f*" in equation (8) will be dropped off from the depth term "*z*" in following discussions. It is noted that this formulation actually describes the frequency signature of the irradiance fluctuations which vary inversely with the square root of the water depth, and is an extension to the previously proposed model [*Fraser et al.*, 1980]. The distribution of *F* factors is highlighted in Figure 3b. According to this example, *F* ranges from 0.5 to 5.3 $m^{1/2}\ s^{-1}$ with the given wave slopes and solar angles.

The above derivations are based on the lighting geometry of a single wave train. The realistic sea surface is composed of a myriad of waves, of a great number of different heights, lengths, directions, and frequencies, juxtaposed as a consequence of local and far-field wind disturbances. Each wave train will produce characteristic foci dependent on the curvature: smaller waves focus the light at shallower depths, while focusing effects by larger waves are more prominent at greater depths. Equation (3) is an estimate for gravity waves only. The smallest capillary waves might impact the underlying irradiance distribution as well [*Stramski and Dera*, 1988] and the measured irradiance field data include information from both the gravity waves and the capillary waves [*Fraser et al.*, 1980; *Nikolayev et al.*, 1972; *Prokopov and Nikolayev*, 1976; *Snyder and Dera*, 1970; *Stramska and Dickey*, 1998]. In the ocean, the light also

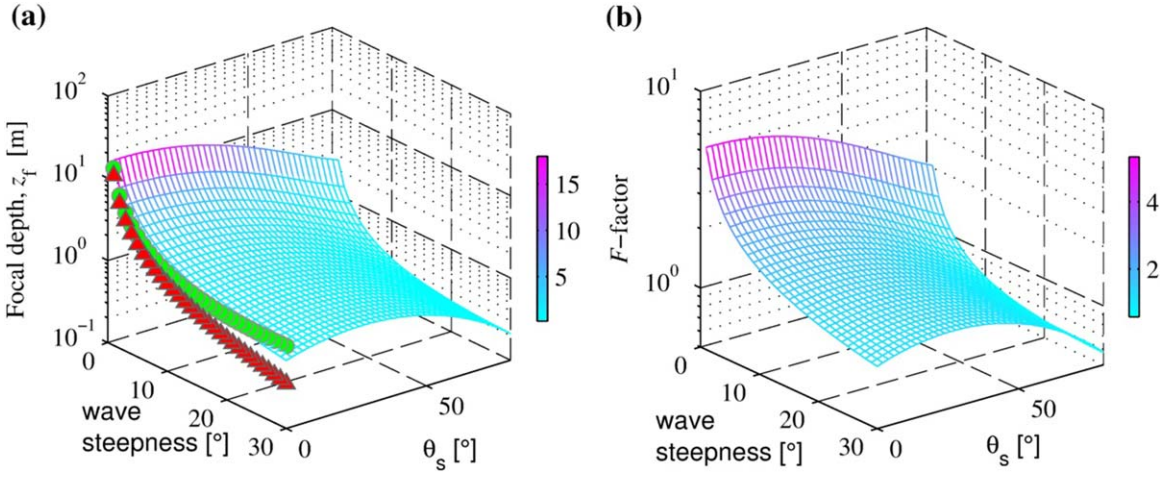

Figure 3. (a) Focal depth of lighting geometry under a modeled sinusoidal sea-surface wave. Two other predictions for vertical incidence are also overlaid according to *Zaneveld et al.* [2001] (denoted in triangles) and *McLean and Freeman* [1996] (denoted as circles); a wavelength of 1 m long is assumed. (b) The *F* factors varying with the solar zenith angle and sea wave slope.

Figure 4. Experiment locations off Hawaii (denoted as red triangles) and in the Santa Barbara Channel, California (denoted as green square).

attenuates with absorption and scattering, so the irradiance measured at the primary foci is usually much higher than those at greater depth.

We have not derived an analytic formulation like equation (8) for the amplitude of irradiance fluctuations. In theory, the variance of the irradiance fluctuations can be very complicated [*Weber*, 2010].

3. Materials and Methods

3.1. Experimental Sites

All data sets used in this study were obtained during "Radiance in a Dynamic Ocean (RaDyO)" field campaigns in the Santa Barbara Channel (SBC), California in September 2008, and in the Pacific Ocean off Hawaii in August and September 2009 (Figure 4). In the SBC, the experiment occurred approximately at the same site in the middle of the channel (34°13.4′N, 119°38.1′W), where the water depth is about 150 m. In the Pacific Ocean, the sampling sites extended westward ∼250 nautical miles from south of the Big Island of Hawaii.

The environmental conditions including the solar zenith angle, wind speed, and sea wave height were different between the Pacific and SBC experiments (Table 1). For example, the large solar zenith angles observed in the SBC result in relatively high sky diffuseness, which is spectrally dependent (Figure 5a). More details of the wind conditions and wave measurements are reported by *Zappa et al*. [2012].

The two seas are representative of optically contrasting waters: the Pacific Ocean water off Hawaii can be treated as Case 1 water, for which the optical properties are dominated by the phytoplankton and related organic dissolved and particulate materials [*Morel and Prieur*, 1977]; the Santa Barbara Channel water generally belongs to Case 2 water whose optical properties are significantly influenced by other decoupled constituents such as inorganic particles and organic materials and their in situ optical properties are summarized in Figures 5b–5d. In the coastal water of the Santa Barbara Channel, the light attenuation in the blue band is very strong due to the absorption of high levels of dissolved organic matter (or colored dissolved organic material, a.k.a. CDOM) and organic detritus and phytoplankton. In contrast, irradiance in the Pacific diminishes slowly in the blue and drops much faster toward longer wavelengths. With no exception, the scattering coefficient decreases toward longer wavelengths.

Table 1. A Summary Over the Irradiance Measurements Used for the Present Study

Property	Santa Barbara Channel	Pacific Ocean
Observation date (UTC)	9–20 Sep 2008	27 Aug to 14 Sep 2009
Observation time (UTC)	∼18:00 and 22:00–23:00	20:00–21:00 and ∼1:00
Observation time (Local Time)	∼11:00 and 15:00–16:00	10:00–11:00 and ∼15:00
Location	34°13.4′N	17°30′–18°00′N
	119°38.1′W	155°30′–159°30′W
Total number of irradiance profiles	9	11
Total number of fixed-position time series observations	5	7
Profile-time series matchups	6	7
Instrument fall velocity, ω_s (m s^{-1})	0.23 ± 0.08	0.31 ± 0.04
Data acquisition rate (Hz)	7	7
K_d (555 nm) (m^{-1})	0.13 ± 0.01	0.07 ± 0.00
Wind speed, U_{10} (m s^{-1})	6.8 ± 1.7	8.6 ± 1.4
Solar zenith, θ_s (deg)	48.2 ± 4.8	32.9 ± 5.4
Significant wave height, H_s (m)	0.75–1.7	1.85–2.35
Dominant wave frequency, f_p (Hz)	0.08–0.3	0.07–0.14
Wave age, C_p/U_{10} (C_p is the phase speed)	0.68–5.36	1.25–2.54

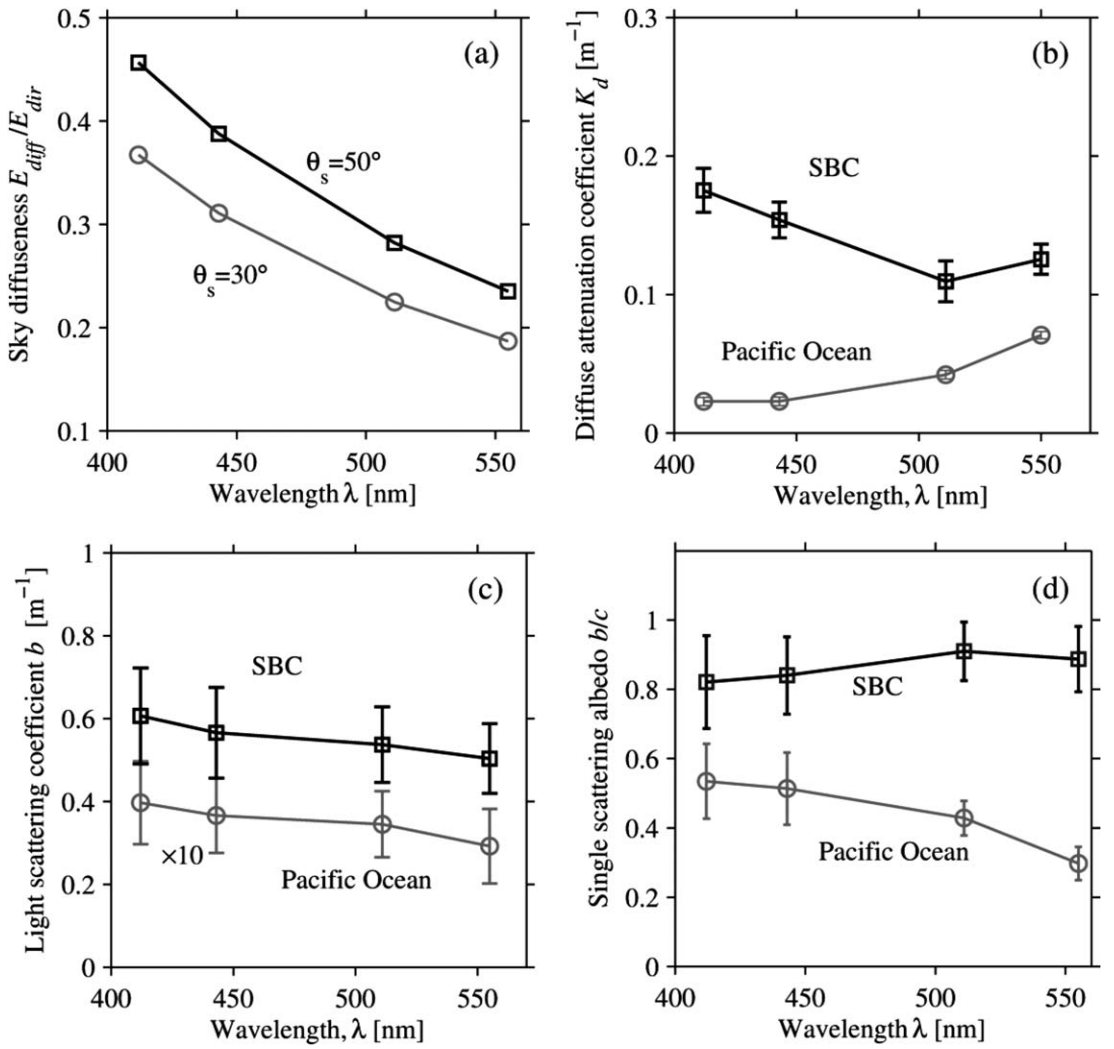

Figure 5. Summary of optical properties. (a) Sky diffuseness. It is computed as the ratio of the diffuse part of the downwelling plane irradiance above sea surface E_{diff} to the direct part of the irradiance E_{dir}, based on the RADTRAN model [*Gregg and Carder*, 1990]. (b) Diffuse attenuation coefficient for downwelling irradiance. (c) Light scattering coefficient. (d) Single scattering albedo.

3.2. Instrument and Deployments

A commercial system was used in our study to measure the irradiance depth profiles, which consists of a coupled irradiance/radiance radiometer (OCR-504I/R, Satlantic LP). As shown in Figure 6, the downwelling irradiance sensor OCR-504I is installed on the wing of a free-fall profiling package [*Wei et al*., 2012]. A CTD sensor to measure the water conductivity, temperature and depth, and a tilt/compass sensor to measure the instrument's roll, pitch, and heading are integrated with this instrument package. All the principal and ancillary sensors are synchronized and are linked to a control computer via a fiber optic cable.

The OCR-504I is a four-channel radiometer recording the downwelling plane irradiance at discrete wavelengths of 412, 443, 511, and 555 nm (FWHM 10 nm). Calibration of the irradiance sensor was carried out according to the ocean color calibration protocols [*Mueller et al*., 2003]. This irradiance collector has surface area of 86 mm^2 and follows a cosine response within its 180° field of view. The system time constant is 0.011 s. It samples instantaneously at a fixed frequency at 7 Hz. The measured irradiance data can be referenced to the instantaneous measurement of inclinations (roll, pitch, and yaw). The sky illumination condition was monitored with a sky reference radiometer (at the same four wavelengths), which is also synchronized with the control computer. Although the radiance camera measured the concurrent radiance distribution along the vertical which can be used to calculate the downwelling plane irradiance [*Lewis et al*., 2011], we did not use them in this study because of its relatively low sampling frequency (4 Hz).

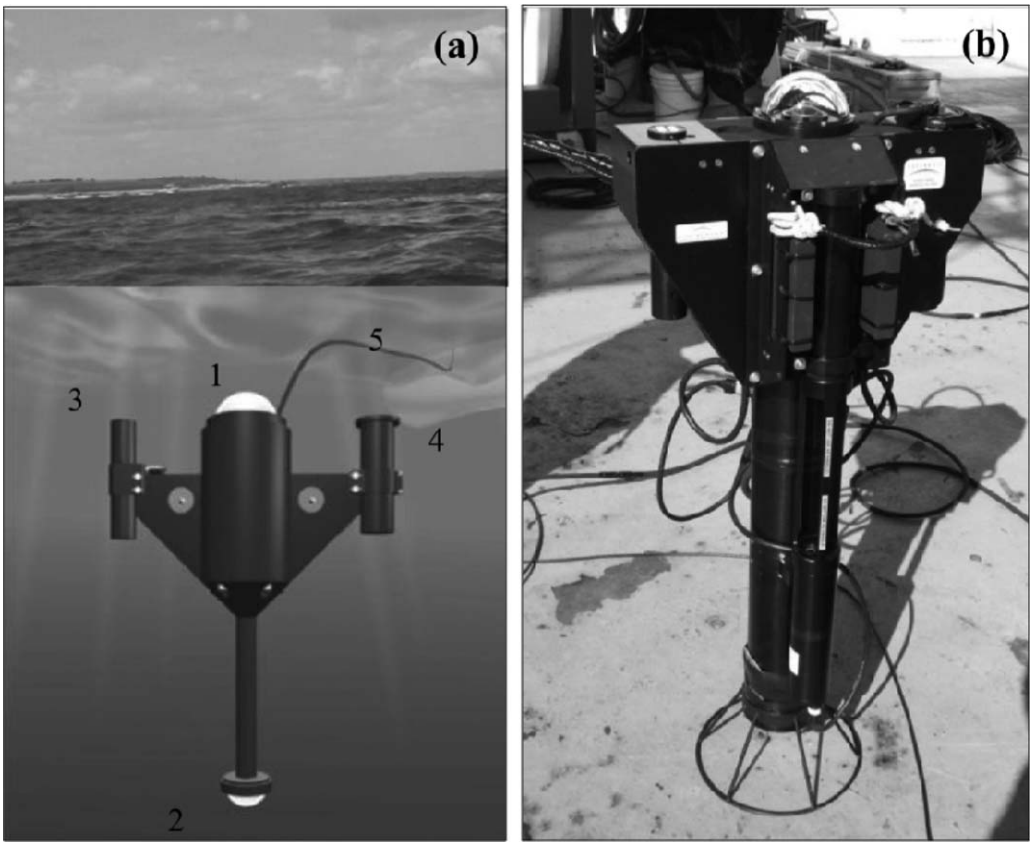

Figure 6. (a) Schematic illustration of the free-fall deployment in water column. (b) A photo of the instrument system standing on board. The instrument package is composed of (1) upward looking radiance camera; (2) downward looking radiance camera; (3) four-channel irradiance/radiance sensor (OCR-504I/R); (4) CTD sensor; and (5) fiber optic cable. Image courtesy of Satlantic LP.

Like commonly used underwater radiometers, the OCR-504I radiometer has a data acquisition rate of $<$10 Hz and hence does not resolve the fastest light flashes that exist. For example, the capillary waves ($<$1.73 cm in length) could play a role in the underwater irradiance field distribution. They may produce "light flashes" with durations as short as tens of milliseconds [*Stramski and Dera*, 1988] in very near surface layers. However, the capillary waves do not generate the dominant signals in the measured light field fluctuations for deeper waters, where it is valid to consider only the gravity waves in equation (8) when modeling the wave-induced irradiance fluctuations and distributions.

Continuous irradiance depth profiles were obtained by releasing the instrument package in a free-fall mode [*Lewis et al*., 1986; *Waters et al*., 1990] at a speed of $w_s = 0.2$–0.3 m s^{-1} in the water column from the deck of the R/V *Kilo Moana*. It usually took $<$3 min to profile the water column from the surface to 40 m depth. The instrument's inclinations were small, with tilts $<5^\circ$ for both yaw and pitch 90% of the time. At some sites, replicate casts were obtained for irradiance depth profiles, which were generally offset in time by about 3 min.

The diffuse attenuation coefficients for the depth profiles, K_d, were determined using the irradiance integration method [*Zaneveld et al*., 2001]. The solar zenith angle, θ_s, was computed from the geographic coordinates and the time of observation [*Reda and Andreas*, 2004].

Irradiance fluctuations were also measured in the more traditional fashion by hanging the instrument package to a small float (25 cm in diameter), which followed the sea-surface displacements and henceforth was not present at a constant depth relative to the mean sea-surface level. We constrained the measurement positions to the first 40 m in the Pacific Ocean and the first 10 m in the Santa Barbara Channel. In the following analysis, these time series will be referred to as "fixed-position" or "fixed-depth" observations. These measurements took place within15–30 min after the irradiance profiling deployments. Changes of solar positions within this short time period are small (no larger than 5°, Table 1).

The upper water column was also profiled with a WET Labs AC9 meter measuring the absorption coefficient, a, and the attenuation coefficient, c, at nine wavelengths including 412, 443, 511, and 555 nm. The scattering coefficient is then given as the difference between the attenuation coefficient and absorption coefficient, $b = c - a$. Deployment and data processing of AC9 are described in *Twardowski et al*. [2012]. In our experiments, the AC9 meter was usually deployed 30 min to 1 h before the OCR-504I radiometer. We determined the mean scattering coefficients by averaging the measurements over 0–40 m in the Hawaiian experiment and 0–10 m in the SBC (see Figures 5c and 5d).

3.3. Irradiance Data Screening

The raw OCR-504I radiometer measurements of irradiance are calibrated to physical units, after applying the immersion coefficients. Both the irradiance depth profiles and fixed-depth irradiance time series undergo the following subsequent data quality checks.

The first check is to verify that the sky radiation is relatively stable during the instrument deployment. The downwelling irradiance above the sea surface, E_s, is derived from the sky reference camera and the OCR-504I surface radiometer recordings. The coefficient of variation (CV), or the ratio of the standard deviation of irradiance to the mean value of irradiance, is then estimated for the sky radiation. Those data sequences having CVs over 5% are eliminated from the following analysis. The second criterion is to ensure that the sky is clear by comparing the ratio of in situ downwelling irradiance above the sea surface with theoretical values at 555 nm. The theoretical irradiance is calculated with the RADTRAN sky radiation model [*Gregg and Carder*, 1990]. The sky is regarded as "clear" only if the ratio is higher than 85%.

The irradiance depth profiles at 20 stations passed the above threshold checks. At 12 stations, the fixed-position time series measurements were also retrieved.

3.4. Irradiance Data Decomposition

The irradiance depth profile data recorded from the OCR-504I radiometer are used as the principal data set in this study.

As a mathematical convenience, the irradiance values were first transformed into natural logarithmic scales. The transformed irradiance profiles were further normalized according to the following relation

$$I_n(z) = \frac{\ln E_d(z) - <\ln E_d(z)>}{<\ln E_d(z)>} \tag{10}$$

where $<\ln E_d(z)>$ is the mean irradiance computed as the linear fit to the log-transformed irradiance values, and $I_n(z)$ is called the normalized irradiance residuals hereafter. For the wavelet transform, the irradiance profiles are treated as equivalent to a (nonstationary) time series, i.e., irradiance sequences with respect to observation time, denoted as $I_n(t)$. The data transformation applied by equation (10) is necessary to ensure that the wavelet transform produces reliable results [*Grinsted et al*., 2004].

To identify the dominant modes of fluctuations in the irradiance depth profiles, the technique of wavelet transformation (WT) was used (Wavelet software was provided by C. Torrence and G. Compo, and is available at http://atoc.colorado.edu/research/wavelets). The wavelet transform is advantageous over Fourier transform (FT) in that it is able to decompose the nonstationary irradiance profile data sequences into the time-period space and the depth-wavelength space, or the depth-period space assuming that the instrument dropping speed is nearly constant. Another advantage of using the wavelet transform is that it is scale independent and there is no need for a predetermined scale that could limit the frequency range. As such, wavelet analysis can likely reveal the evolution of dominant modes of irradiance fluctuations with depth and/or time. A summary of wavelet analysis in geophysics has been given by *Torrence and Compo* [1998]. The continuous wavelet transform with uniform time steps Δt is defined as the convolution of I_n (t) with the wavelet function $\psi(t)$,

$$W_n(S) = \sum_{n'=0}^{N-1} I_n \psi^* \left[\frac{(n'-n)\Delta t}{S} \right] \tag{11}$$

where n is the localized time index, N is the number of points in the time series, and the asterisk indicates the complex conjugate. Equation (11) gives a complex continuous wavelet transform (CWT). The squared modulus of the CWT, $|W_n(S)|^2$, is used in this context for convenience.

The choice of wavelet function in this study was the Morlet wavelet, a complex nonorthogonal wavelet consisting of a sinusoid modulated by a Gaussian envelope

$$\psi(t)=\pi^{-1/4}\exp\left[i\omega_0\left(\frac{t}{S}\right)\right]\exp\left[-\frac{t^2}{2S^2}\right] \tag{12}$$

where t is the time (unit: s), S is the wavelet scale (unit: s), and ω_0 is the nondimensional frequency. In our analysis, the nondimensional parameter $\omega_0 = 6$ was used, such that there are three oscillations within the Gaussian envelope and the wavelet scale S is almost equal to the Fourier period, i.e., $T = 1.03 \times S$. We use the term "period" hereafter to describe the wavelet transform. The reciprocal of the period is the frequency, f, with the unit of Hertz.

To determine the significance of the wavelet spectra, a background red noise process was constructed and modeled as a first-order univariate autoregressive (AR1, or Markov) process

$$x_n=\alpha x_{n-1}+\varepsilon_n \tag{13}$$

where α is the lag-1 autocorrelation, $x_0 = 0$, and ε_n is taken from Gaussian white noise. The normalized power spectrum of this AR1 process is defined as

$$P_k=\frac{1-\alpha^2}{1+\alpha^2-2\alpha\cos\left(2\pi k/N\right)} \tag{14}$$

where $k = 0 \ldots N/2$ is the Fourier frequency index, and α is the lag-1 autocorrelation estimated from the normalized irradiance residuals. The statistical significance of the wavelet power was then assessed relative to the null hypothesis that the signals (normalized irradiance residuals $I_n(t)$) have a mean power spectrum as P_k; if a peak in the wavelet power spectrum is significantly above the background spectrum, it can be assumed to be a true feature. To determine the 95% confidence level (significant at 5%), the background spectrum of equation (14) was multiplied by the 95th percentile value for χ^2_2, which implies chi-square distribution with two degrees of freedom.

Based on the computed wavelet spectrum (see Figure 8), we derived the dominant frequency by locating the frequency with a local maximum variance value. The identified frequencies are only accepted if the estimated confidence level is above 95%. A special relationship is determined between the variance of irradiance residuals, Var$[I_n(\lambda,z)]$, and the coefficient of variation. The derivation starts with equation (10). We first take the variance for both sides of this equation, which is described as

$$Var[I_n(\lambda,z)]=\frac{Var[\ln E_d(\lambda,z)]}{<\ln E_d(\lambda,z)>^2} \tag{15}$$

The denominator is already known in our analyses. The numerator can be further transformed into the following relation by considering the second-order Taylor expansion,

$$Var[I_n]=\frac{Var[E_d]}{(\mathrm{E}[E_d])^2}\cdot\frac{1}{<\ln E_d>^2} \tag{16}$$

In the above equation, E$[E_d]$ denotes an expectation of the downwelling plane irradiance, and the dependence on depth and wavelength has been omitted for simplicity. Note that the first part on the right-hand side of equation (16) actually gives the square of the CV at depth z. We derived the continuous CV profiles based on this scheme for each irradiance depth profile.

For the fixed-position irradiance time series data, we used spectral analysis to derive the power spectral density. The Parzen's windowing technique was adopted. The dominant frequency f_p was determined as the one which gives the maximum variance. The coefficient of variation was also computed.

Considering that the capillary waves likely dominate the irradiance fluctuations at very near surface regions, we constrained our data analyses to water depths deeper than 1 m.

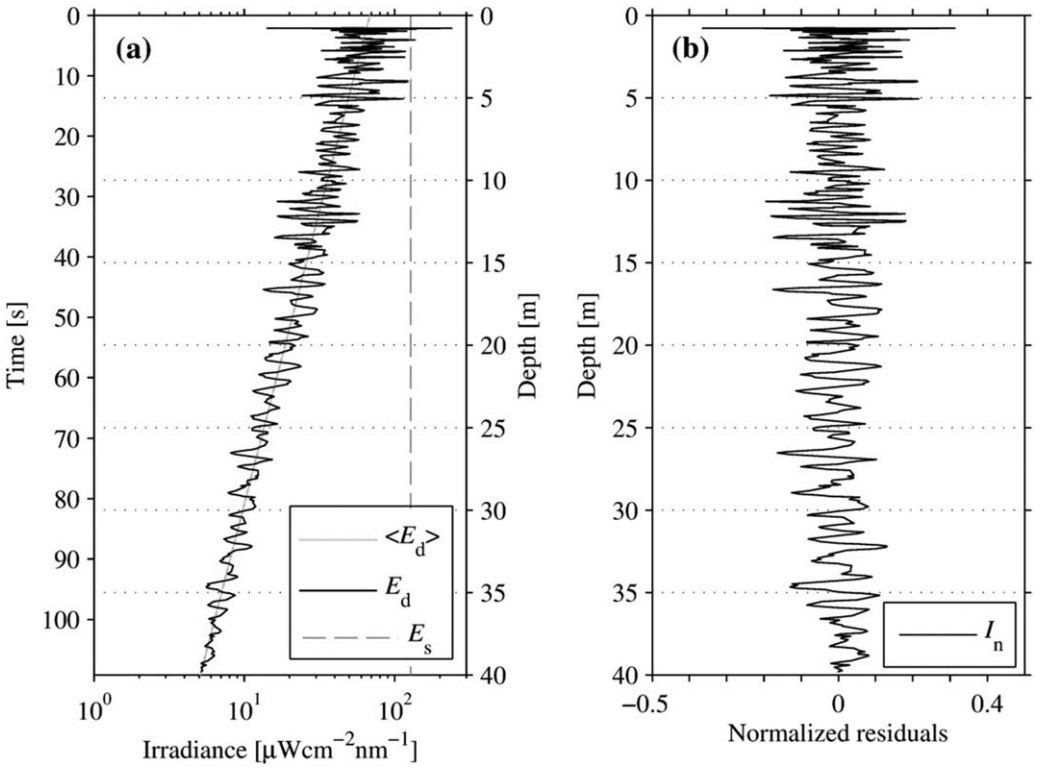

Figure 7. (a) Irradiance depth profiles ($\lambda = 555$ nm) in the Pacific Ocean under clear sky. (b) Normalized irradiance depth profile $I_n(555)$. The irradiance profiles were measured on 5 September 2009, 00:30 UTC; the instrument package descends at a speed of 0.45 m s^{-1} in water, with a data acquisition frequency of 7 Hz; clear sky; wind speed 10 m s^{-1}; sea surface is dominated by waves of 1.5–2 m high.

3.5. Error Analysis

The parameters (CV and dominant frequency f_p, and also the expectation of the downwelling plane irradiance) have been so computed from both the irradiance profiles and the fixed-position irradiance time series. Two statistical measures were used to assess the differences between the parameters derived from the irradiance profiles and those computed from the fixed-position time series, namely the root-mean-square error (RMSE) and the mean relative error (ε). They are defined as follows

$$RMSE = \sqrt{\frac{1}{N}\sum_{i=1}^{N}\left[\log_{10}(P)_i - \log_{10}(Q_i)\right]^2} \tag{17}$$

$$\varepsilon = \frac{1}{N}\sum_{i=1}^{N}\frac{|P_i - Q_i|}{Q_i} \times 100 \tag{18}$$

where P_i is the quantity derived from measured profiles and Q_i refers to the quantity from the fixed-position time series. N is the total number of valid retrievals. In addition, regress analysis was also performed where necessary to derive the regression slope, intercept, and coefficient of correlation.

4. Results

4.1. Example Data of Irradiance Depth Profiles

An example irradiance depth profile is presented in Figure 7 for the clear oceanic waters. The mean irradiance, $<E_d>$, is described by an exponential fit to the original irradiance data (E_d) as indicated in equation (1). As illustrated in the plots, the irradiance sequences are functions of water depth as well as the observation time.

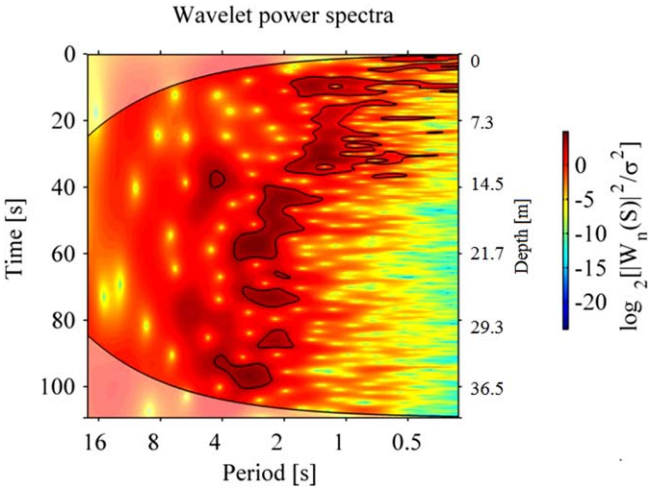

Figure 8. Normalized continuous wavelet power spectra, $\log_2[|W_n(S)|^2/\sigma^2]$, for the irradiance residuals I_n at $\lambda = 555$ nm. The normalization by σ^2 gives a measure of the power relative to white noise; the thick black contour represents the 95% confidence interval; the cone of influence (COI) is depicted by a transparent patch. The irradiance profile, E_d, was collected in clear Pacific Ocean off Hawaii, on 5 September 2009, 00:30 UTC (same data as Figure 7).

The data sequences of irradiance depth profiles describe a unique yet nonstationary process, in which both the irradiance mean and variance vary with depth and time. The instantaneous irradiance oscillates about the mean and is slightly positively skewed. The deviations of the instantaneous irradiance about the mean irradiance profile are generally attenuated with water depth [also see *Siegel and Dickey*, 1988; *Zaneveld et al*., 2001]. The deviations of irradiance measurements from the mean irradiance $<E_d>$ are referred to as "the irradiance fluctuations" in depth profiles hereafter. According to the data in Figure 7, the distance (Δz, in terms of water depth) between two neighboring local maxima or minima in the irradiance profiles actually increases with water depth. For example, Δz is about 0.5 m at depth of 5 m, but changes to a larger value of $\Delta z = 1.5$ m, at a position of 22 m, corresponding to the time difference, ΔT, increasing from 1.1 to 3.3 s at the given drop velocity. It is founded that the normalized irradiance residuals I_n can be roughly approximated by a normal distribution model (analysis results not shown). Also note that the probability distribution of I_n does not affect the subsequent wavelet decomposition [*Torrence and Compo*, 1998].

4.2. Example Wavelet Spectra of Irradiance Profile

The wavelet spectra of the detrended and normalized irradiance sequence $I_n(t, z, 555\text{ nm})$ in the time-period domain are illustrated in Figure 8, in which the absolute value squared of the transform is normalized by the total variance. The data were taken from the Hawaii experiment. The spectra correspond to the irradiance depth profile demonstrated in Figure 7. The *x* axis gives the Fourier period, while the *y* axis describes the evolution of observation time. The observation time scales to the water depth through the drop velocity (not shown in figure). The artifacts with the spectra are that the wavelet is not completely localized in time, and may be subjected to the edge effects. We have used the cone of influence (COI) approach [*Grinsted et al*., 2004] to define such areas in Figure 8, where the black contour encloses regions of >95% confidence for a red-noise process. The spectra show a characteristic distribution of periods. Wavelet transform in the time-period domain allows for identification of the local dominant periods of irradiance fluctuations, at which the power in the spectra reaches the maximum and is above the 95% confidence level. The dominant periods increase from 0.25 s near the surface to about 4 s at depth of 40 m. The inverse of the period gives the dominant temporal frequency f_p, which decreases with water depth.

4.3. Depth Distribution of Dominant Frequency

The relationship between the dominant frequency of irradiance fluctuations and water depth is described in this section. Data points are resampled at every half meter in the wavelet evolutionary spectra, and those with confidence levels lower than 95% are discarded. Figure 9a shows an example of the frequency distribution of irradiance fluctuations at 555 nm from the Pacific Ocean, representing the sea state under high winds of ~9 m s^{-1} and significant sea wave heights of 2.1 m. The model of equation (8), $f_p = F \times z^{-0.5}$, where $z > 0$, is satisfactorily fitted to the resampled frequency data, with the *F* factor equal to 1.614 $m^{1/2}$ s^{-1} and the coefficient of multiple determination $r^2 = 0.574$.

The ensemble of such fitted f_p profiles from the Pacific Ocean is displayed in Figure 9b. These profiles represent the irradiance observations taken under similar environmental conditions, that is, high winds

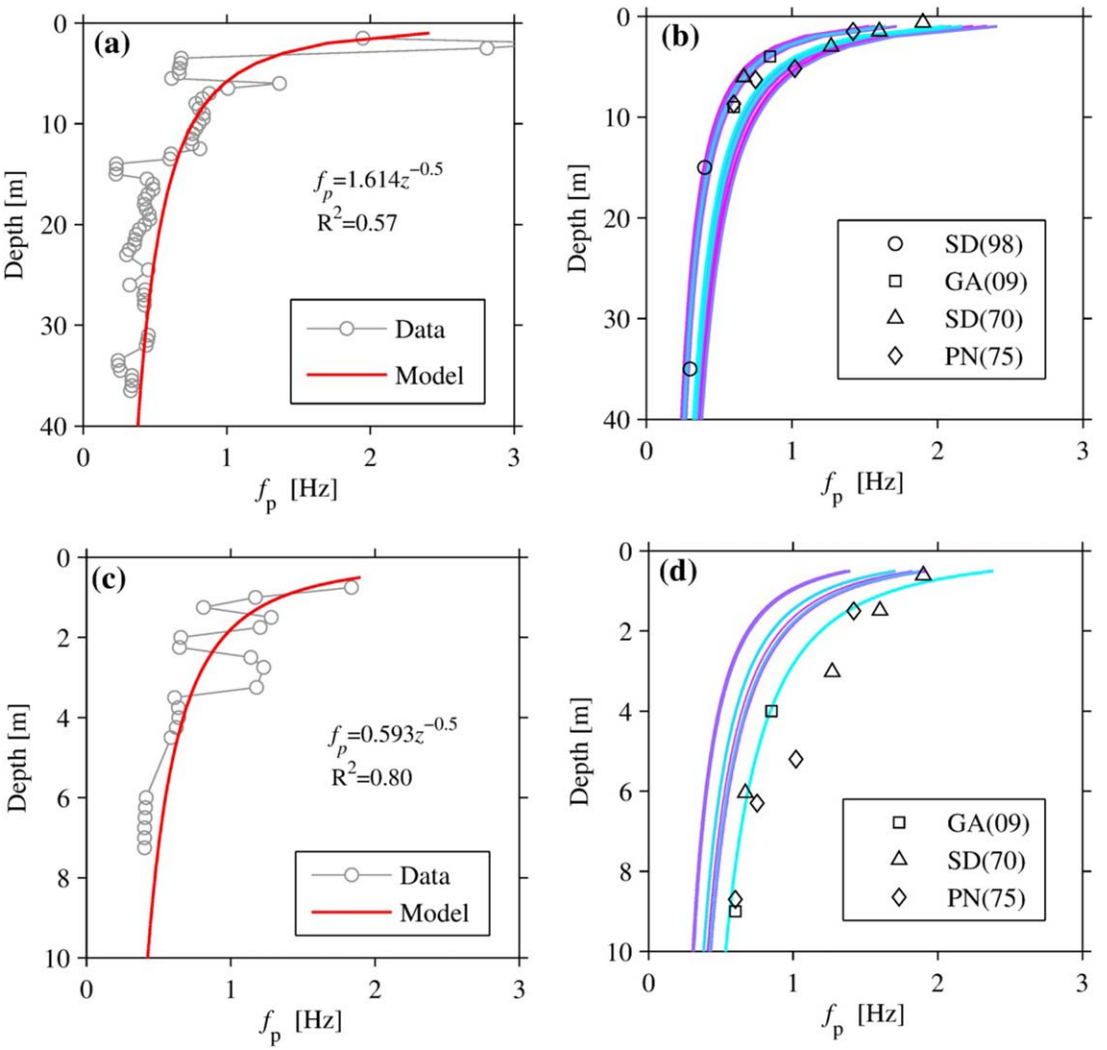

Figure 9. Depth evolution of the dominant frequency of the irradiance fluctuations derived from irradiance profiles (555 nm) measured under clear skies. (a) Example of model fitting for the Pacific Ocean data, which were retrieved on 5 September 2009, with wind speed 9.2 m s^{-1} and solar zenith angle 32°; the significant height of sea waves was 2.1 m. (b) The fitted f_p distributions in the Pacific Ocean; a total of 12 measured irradiance depth profiles are processed for the model fitting and represented by lines in different colors. (c) Example model fitting of the Santa Barbara Channel data, which were recorded on 14 September 2008, with wind speed 7.7 m s^{-1} and solar zenith angle 54°; the significant height of sea waves was 0.85 m. (d) A family of the f_p profiles in the Santa Barbara Channel; a total of nine irradiance depth profiles are used for the model fitting and represented by lines in different colors. The historical f_p data are overlaid for comparison. SD(98): λ = 555 nm, θ_s = 30°, by *Stramska and Dickey* [1998]; GA(09): λ = 510 nm, θ_s = 20–85°, by *Gernez and Antoine* [2009]; SD(70): λ = 525 nm, θ_s = 35–44°, by *Snyder and Dera* [1970]; PN(75): λ = 525 nm, θ_s = 36–57°, by *Prokopov et al.* [1975].

(U_{10} = 5–10 m s^{-1}) and medium solar zenith angles (θ_s = 27°–35°). The fitted F factors have a mean value of 2.06 with a standard deviation of 0.41, i.e., $F = 2.06 \pm 0.41$ $m^{1/2}$ s^{-1}.

Figure 9c presents an example for the f_p profile data measured in the Santa Barbara Channel, and Figure 9d illustrates the ensemble of fitted f_p profiles in the Santa Barbara Channel. The F factors are found to be generally lower than those observed in the Pacific, with a mean value of 1.31 and with the standard deviation of 0.20, i.e., $F = 1.31 \pm 0.20$ $m^{1/2}$ s^{-1}. Historical data [*Gernez and Antoine*, 2009; *Prokopov et al.*, 1975; *Snyder and Dera*, 1970; *Stramska and Dickey*, 1998] are also overlaid in the plot, which are slightly higher than our deviations in the Santa Barbara Channel. Such differences are mainly due to the different environmental conditions met in the field experiments, such as the different solar zenith angles.

4.4. Depth Distribution of Coefficient of Variation

The variance Var(I_n) is required for the derivation of the coefficient of variation (equation (16)). In our analysis, the variance is determined as the average over bands of 0.29 to 4 s for each depth based on an objective examination of the wavelet spectra of the irradiance depth profiles; 3.5 Hz (0.29 s in period) roughly

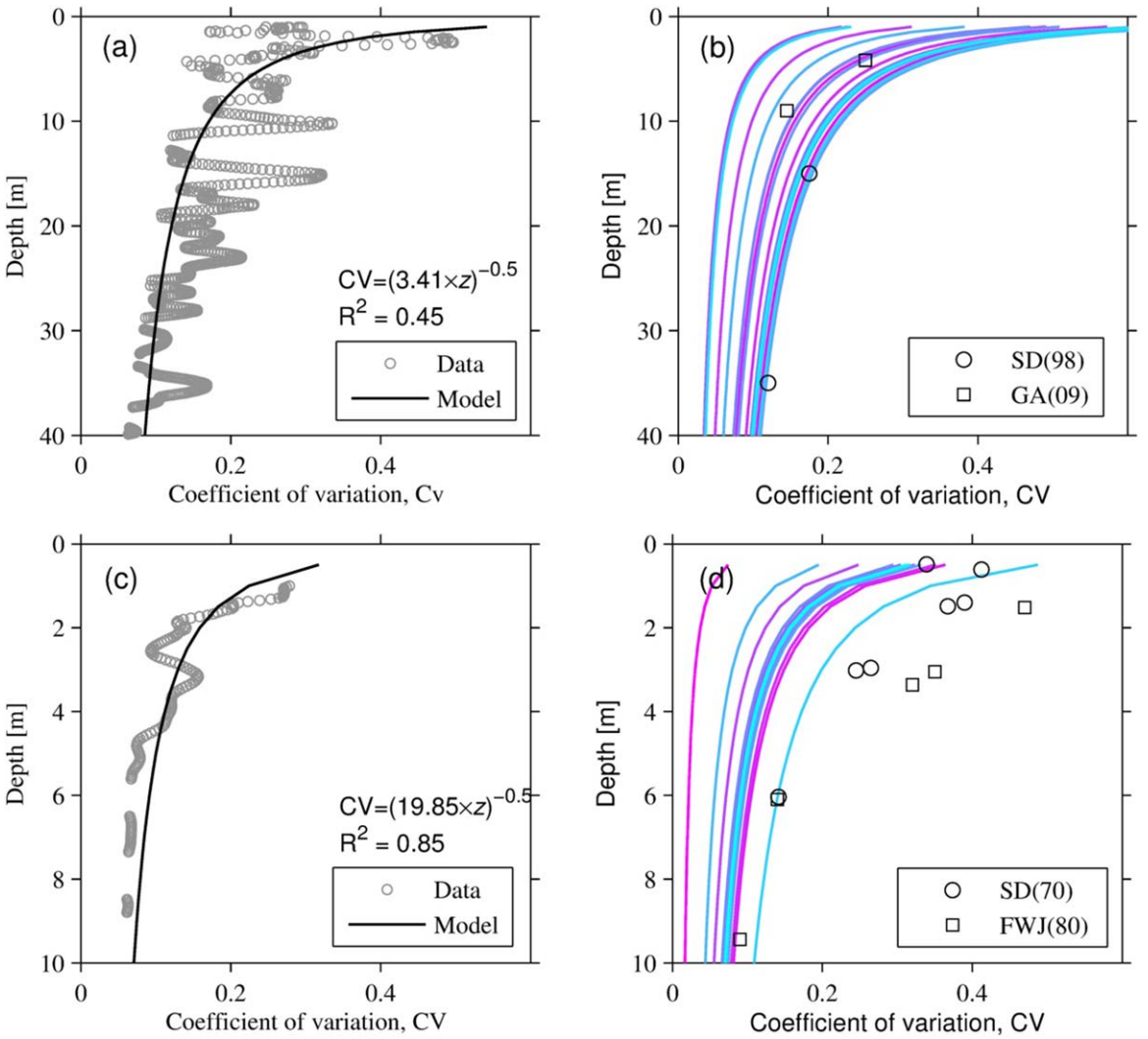

Figure 10. Depth evolution of the coefficient of variation of the irradiance fluctuations derived from irradiance profiles (555 nm) measured under clear skies. (a) Example of model fitting of the CV distribution in the Pacific Ocean; same profile was used as Figure 9a. (b) Ensemble of fitted CV profiles in Pacific Ocean represented by lines in different colors. (c) Example of model fitting of the CV distribution in the Santa Barbara Channel; same irradiance profile was used as Figure 9c. (d) A family of the CV profiles in the Santa Barbara Channel represented by lines in different colors. Historical CV data are also shown for comparison. SD(98): $\lambda = 555$ nm, $\theta_s = 30°$, by *Stramska and Dickey* [1998]; GA(09): $\lambda = 510$ nm, $\theta_s = 20°–85°$, by *Gernez and Antoine* [2009]; SD(70): $\lambda = 525$ nm, $\theta_s = 26°–44°$, by *Snyder and Dera* [1970]; FWJ(80): $\lambda = 525$ nm, $\theta_s = 23°$, by *Fraser et al*. [1980].

corresponds to the Nyquist frequency of our data, and 0.25 Hz (4 s in period) is the dominant frequency over 5% significance found at depths of 40 m in the Pacific Ocean (see Figure 9). We also note that only the variance beyond the COI (that is free from edge effect) and above 5% significance level in the wavelet spectra is considered in the variance integration. Before the procedure was started to compute the coefficient of variation, the sufficiency of the chosen frequency band was first evaluated. It is found that >98% of the variance in the original series can be accounted for over the frequency band 0.25–3.5 Hz.

The evolution of the coefficient of variation of the irradiance fluctuations with water depth is illustrated in Figures 10a and 10c. Our analysis shows that the coefficients of variation generally decrease with water depth; this finding agrees with previous reports from fixed-depth irradiance time series data [e.g., *Darecki et al*., 2011; *Fraser et al*., 1980; *Gernez and Antoine*, 2009; *Prokopov et al*., 1975].

Several simple models are tested for description of the depth evolution of the coefficient of variation, including the exponential function and polynomial functions and a similar formulation with equation (8),

$$CV = (K_{cv} z)^{-1/2} \qquad (z > 1) \tag{19}$$

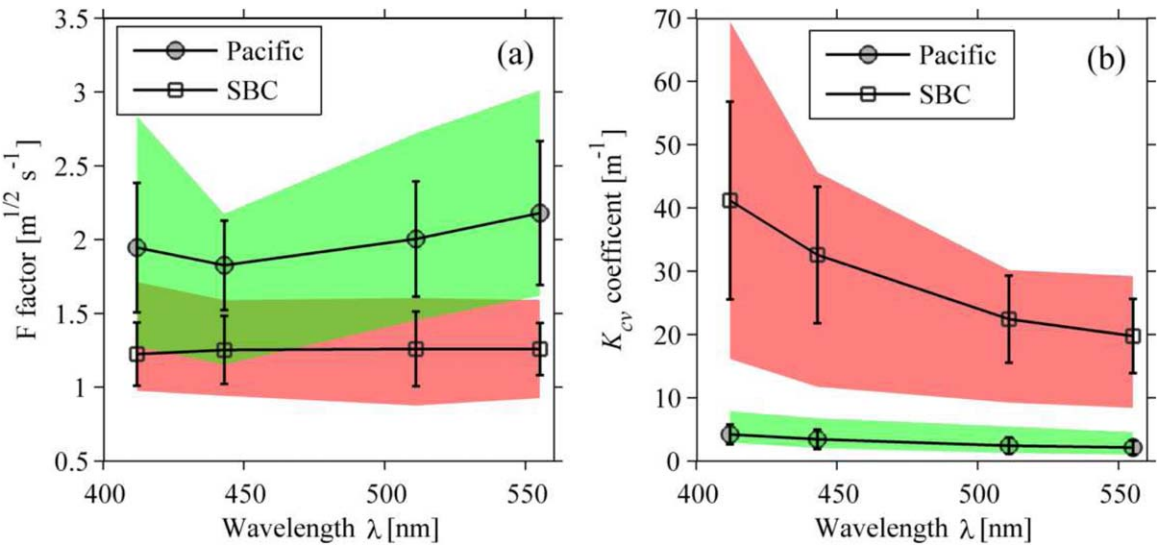

Figure 11. Spectral dependence of irradiance fluctuations in the measured irradiance depth profiles under clear skies. The mean values are denoted as circles (for Pacific Ocean data) and squares (for SBC data); the error bars represent the standard deviations of the data. The shaded areas (green for Pacific data, and red for SBC data) describe the upper and lower limits of the observed parameters.

where K_{CV} (unit: m^{-1}) is the only parameter determining the coefficient of variation besides the water depth z. It is found that the model of equation (19) can satisfactorily fit most of the profiles in the two sea surface waters with the coefficient of determination often >0.4. Hereafter, K_{cv} is called the attenuation coefficient for CV.

Families of fitted curves of the coefficients of variation as a function of water depth are displayed in Figures 10b and 10d, representing the data from the Pacific and the Santa Barbara Channel, respectively. On average, the attenuation coefficients for CVs in SBC are greater than those in the Pacific Ocean. Some published data is superimposed in these two plots for a qualitative comparison, which also describes a similar decreasing trend with the water depth. Note that the CV can be sensitive to water turbidity as well as solar zenith angles, etc., according to the fixed-depth time series data [e.g., *Gernez and Antoine*, 2009].

4.5. Spectral Dependence of Irradiance Fluctuations

The depth distributions of the dominant frequency and the coefficient of variation have been presented so far for one wavelength at $\lambda = 555$ nm, and their optical spectral dependence is now examined for all four wavelengths including 412, 443, 511, and 555 nm. These spectral irradiance data were measured simultaneously by the OCR-504I radiometer.

We have not observed apparent and consistent trends in the spectral F factor based on individual irradiance profiling deployment (data not shown). The F factors derived from the Pacific Ocean and the Santa Barbara Channel are pooled in Figure 11a. The SBC data give a rather flat distribution of F factors over these spectral bands (ANOVA, F ratio = 0.06, $p = 0.982$). Although the mean F factor reaches a low value at 443 nm and then increases a bit, the spectral dependence is not significant either for the Pacific Ocean data (ANOVA, F ratio = 1.03, $p = 0.394$).

Unlike the frequency content, the amplitudes of the irradiance fluctuations show a systematic variation with the wavelength according to individual irradiance profiling deployments (data not shown). All the derived K_{cv} factors are summarized in Figure 11b, which shows a monotonous decrease of the mean K_{cv} factors with the light wavelength. This variability is significant for both the Pacific data (ANOVA, F ratio = 3.78, $p = 0.021$) and the SBC data (ANOVA, F ratio = 8.75, $p < 0.001$). According to equation (19), the spectral variability of K_{cv} means the coefficient of variation is actually increasing with the optical wavelength.

4.6. Data Validation and Repeatability of Irradiance Profile Derivations

In previous sections, we have been focusing on the signatures of light field fluctuations in the continuous irradiance profiles. We now present the validation of the irradiance depth profile derivations first against

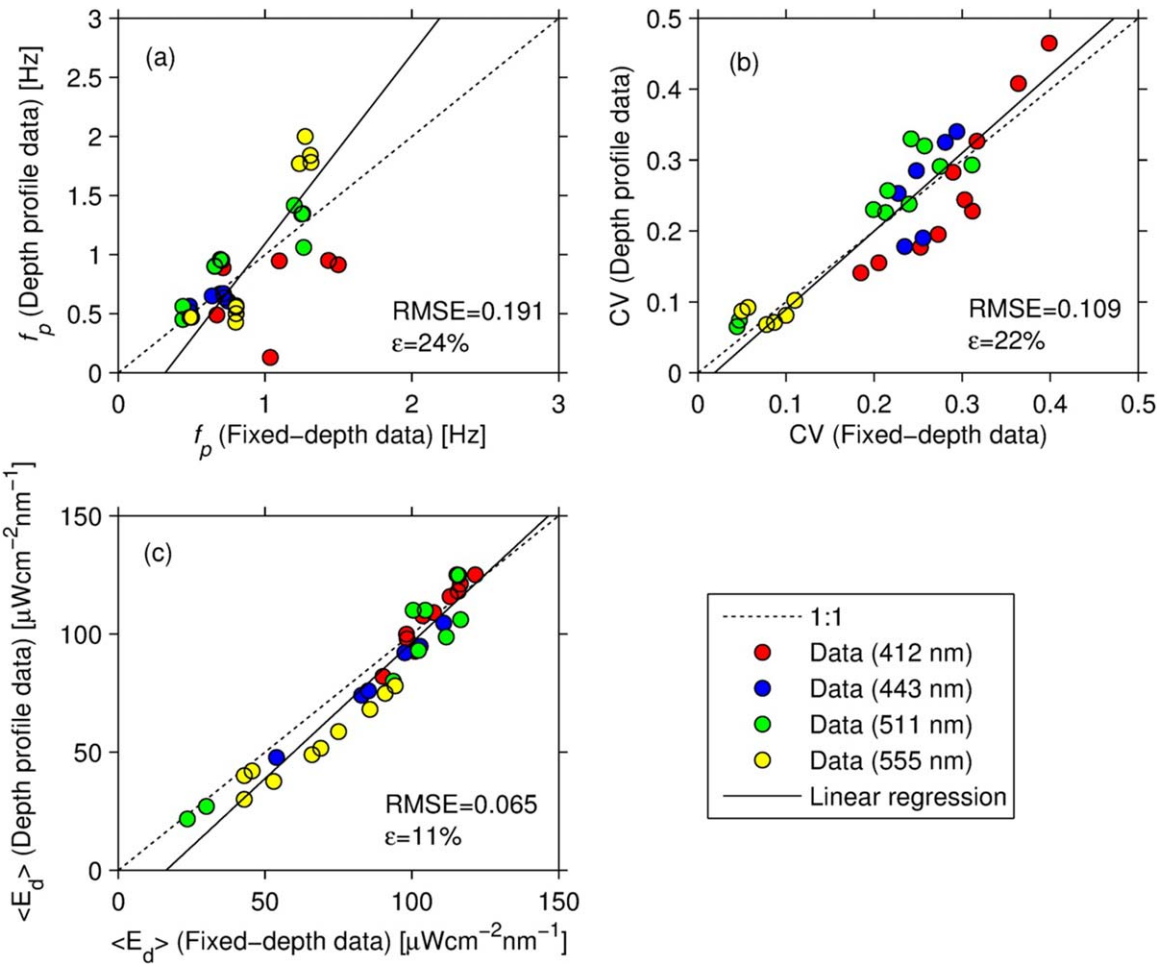

Figure 12. Scatter plots of signatures derived from irradiance depth profiles and fixed-position time series under clear skies. (a) Dominant frequency f_p derived within water depths of 1–13.5 m. (b) Coefficient of variation derived within water depths of 2.3–13.5 m. (c) Mean irradiance derived within water depths of 1–13.5 m. The root-mean-square error and the mean relative error are also indicated for the depth profiles' derivations and time series derivations.

the independent measurements of irradiance variability at fixed depths and second by examination of replicate profiles.

For the first comparison, statistics derived from fixed depth deployments were compared with those derived from a profile collected within 15–30 min and under clear skies. The OCR-504 radiometer suspended at fixed depths often underwent a little larger inclination (but usually $<10^{\circ}$) than those of depth profiling data. We first checked for the potential impact of the sensor's inclinations on the irradiance data using the camera-measured radiance distribution (data not shown). According to our observation, the absolute difference induced by the instrument's inclinations is $<5\%$ with regard to the mean, standard deviation and CV of the irradiance time series; this is consistent with theoretical predictions [*Gege and Pinnel*, 2011].

We compared parameters derived from the irradiance depth profiles with those measured by suspending the instrument at fixed depths below the sea surface in Figure 12. A summary of the error statistics is given in Table 2. The dominant frequencies determined from the two data sets agree reasonably well with each other (Figure 12a) with no significant difference according to a paired t test ($t = -0.1$, and $p = 0.92$, at $\alpha = 5\%$ significance level, $\varepsilon = 24\%$). For the coefficient of variation (Figure 12b), the two methods have also generated consistent results ($t = 0.58$, and $p = 0.56$, at $\alpha = 5\%$ significance level, $\varepsilon = 22\%$). As an additional result, we derived the mean irradiance $\bar{E}_d$ from the fixed-depth irradiance time series by taking the exponential of the mean of the log-transformed irradiance. In Figure 12c, the profiles generate an average irradiance at depth that is not significantly different from that derived from the fixed-position time series; the

Table 2. Error Statistics Between the Profiles-Derived Parameters and Fixed-Position Time Series-Derived Parameters[a]

	Paired *t* Test ($\alpha = 0.05$)			Linear Regression					
Parameters	*t*	*p* Value	CI	R^2	Slope	Intercept	RMSE	*E* (%)	*N*
f_p	−0.1	0.92	−0.18, 0.17	0.51	1.60	−0.51	0.191	24	36
CV	0.58	0.56	−0.03, 0.06	0.81	1.10	−0.02	0.109	22	32
$<E_d>$	0.93	0.35	−6.9, 19.1	0.94	1.15	−18.8	0.065	11	40

[a]All data at four spectral bands (412, 443, 511, and 555 nm) are pooled together for the analysis.

paired *t* test is insignificant ($t = 0.93$, and $p = 0.335$, at $\alpha = 5\%$ significance level, $\varepsilon = 11\%$). For the mean irradiance, we have corrected for the variation of above-surface irradiance E_s even though it is small.

We also examined replicate irradiance profiles taken by the free-fall OCR-504I unit. Each pair represents repeated profiles with the same environmental conditions including the wind speed and solar zenith angle and within 15–30 min of each other. With regard to the dominant frequency, the pairs of derived *F* factors show no significant difference with each other after the paired *t* test ($p = 0.117$, $t = 1.609$, $df = 35$, $\alpha = 0.05$). Since the coefficient of variation is dependent on wavelength (refer to previous figures), we tested the repeatability of the paired K_{cv} coefficients with respect to each wavelength and find that *p* values are all >0.325 and insignificant at significance level $\alpha = 0.05$. The K_{cv} parameters are also pooled together for the paired *t* test, which shows the paired data again are not significantly different. The paired *t* test results for the comparison are summarized in Table 3.

5. Discussion

We have examined for the first time the fluctuating signals in the downwelling plane irradiance depth profiles recorded by a profiling radiometer in the upper ocean using the wavelet transform method where the irradiance depth profiles (time-stamped data sequence) are treated as nonstationary time series. Unlike data from fixed-depth deployments [*Darecki et al*., 2011; *Fraser et al*., 1980; *Gernez and Antoine*, 2009; *Prokopov et al*., 1975; *Snyder and Dera*, 1970; *Stramska and Dickey*, 1998], the irradiance depth profile is a realization of the dynamic light field under the influence of surface waves but along the vertical. The derived light field statistics from the depth profiles hence allow derivation of quantitative spatial information, including the vertical variation in the dominant frequency and coefficient of variation of the light field fluctuations.

In our study, the frequency of irradiance fluctuations is observed to diminish in the vertical (Figure 9). Decreases in the dominant frequency with depth have been described before. In a qualitative sense, and assuming that subsurface fluctuations are due to sea-surface waves with varying periods, it is clear that large waves with longer periods have a dominant influence in deeper waters while small waves of short periods are more important sources of variability in shallower regions beneath the sea surface. This is consistent with ray models such as equation (4) in this study and those proposed before [*Walker*, 1994; *Zaneveld et al*., 2001] and can readily be observed in published irradiance profile data [*Schubert et al*., 2001; *Zaneveld et al*., 2001; *Zibordi et al*., 2004]. We found, somewhat surprisingly, that a rather simple model of surface wave focusing (equation (8)), which predicts an inverse square root dependency on depth, could explain a large fraction of the vertical variance in the dominant frequencies of irradiance fluctuations in the upper ocean. Furthermore, the model can explain to a remarkable degree similar observations reported in the

Table 3. Summary of Paired *t* Test for the Comparison of the Two Matched *F* Factors and K_{cv} Factors Derived From the Two Irradiance Depth Profiles[a]

	F Factor			K_{cv} Factor		
Light Wavelength λ (nm)	*p* Value	*t*	*df*	*p* Value	*t*	*df*
412	0.325	1.048	8	0.876	−0.161	8
443	0.732	0.355	8	0.747	0.335	8
511	0.383	0.923	8	0.780	−0.289	8
555	0.476	0.748	8	0.901	−0.128	8
All data[b]	0.117	1.609	35	0.896	−0.132	35

[a]The paired *t* test is carried for both sides at the significance level $\alpha = 0.05$.
[b]All spectral data (412, 443, 511, and 555 nm) are considered together.

past from optical measurements taken from moorings at fixed depths below the surface, particularly for clear waters (Figure 9b) [e.g., *Fraser et al*., 1980; *Gernez and Antoine*, 2009; *Snyder and Dera*, 1970; *Stramska and Dickey*, 1998].

We note that the parameter *F* in our model varies with environmental conditions such as the solar zenith angle and wave steepness [also see *Nikolayev et al*., 1972]. In the original formulation of equation (9), for example, the *F* factor depends on the wave steepness *Hk*/2 for a constant solar zenith angle θ_s. The data points scattered about the fitted curves in Figures 9a and 9c can be ascribed to the changing wave steepness of the instantaneous topography of sea surface. The model fitting with an estimation of *F* factor then relates the light field dynamics to the average steepness of surface waves. Variation of sea wave height and/or wave period (wave length) and the wind speed causes changes in the average steepness, and henceforth variation in the *F* factor. According to *Kumar et al*. [2009], the wave steepness is associated with several critical parameters of the wave field, including the significant wave height, dominant period, and wind speed, $\delta = \omega_p^{5/2} H_s U_{10}^{1/2} g^{-3/2}$, where δ is the wave steepness parameterized as the ratio of *H* to Λ, ω_p is the dominant angular frequency, and H_s is the significant wave height. Based on the estimated *F* factors, equation (9) can be used to estimate the wave steepness (ratio of wave height *H* to wavelength Λ) of 0.099 and 0.117 for the Pacific experiment and SBC experiment, respectively. Direct measurements of the surface wave height field from the laser altimeter [*Zappa et al*., 2012] resulted in derived $\delta = 0.094$ and $\delta = 0.195$ for the Pacific and SBC experiments, respectively, which is in remarkable agreement with our results based solely on optical variation.

With equation (16), we calculated the variance profile Var[I_n] by averaging the variance between 0.29 and 4 s periods from the wavelet spectrum, which are found to represent >95% of the variance. The coefficient of variation is then described as an inverse square root function of the water depth (equation (19); Figure 10). As with the dominant frequency, the simple model explains as well a large amount of the vertical variance in other studies which utilized fixed-depth time series data [e.g., *Darecki et al*., 2011; *Fraser et al*., 1980; *Gernez and Antoine*, 2009; *Snyder and Dera*, 1970; *Stramska and Dickey*, 1998], but provides quantitative details along the water column of interest. Although the occurrence of local maximum CV at shallow depths is theoretically possible [*Weber*, 2010], our depth-profile derivations only occasionally exhibit such maxima in the coefficient of variation near the water surface (e.g., Figure 10c). So our CV model of equation (19) does not predict the occurrence of maxima at shallowest depths.

There are several issues which merit further discussion. First, one may have noted that the light flashes caused by the small capillary are characteristic of frequencies much higher [e.g., *Darecki et al*., 2011] than our sampling frequency. However, the dominant frequency of irradiance fluctuations as derived from the power spectra of irradiance data rarely exceeds 3.5 Hz (the Nyquist frequency of our radiometer). Rather, it usually falls within a range of low-frequency bands, for example, ~1–1.2 Hz within water depths of 0.5–2 m [*Dera and Stramski*, 1986] and 1.1–2.5 Hz within 0.86–2.84 m water depths [*You et al*., 2010]. So our instrument with the sampling frequency of 7 Hz is sufficient to capture the dominant signals in the temporal domain, but to be conservative, would put more confidence in the data >1 m of depth.

Another issue associated with the sampling frequency is its potential influence on the variance of measured irradiance fluctuations at the very shallow depths [*Darecki et al*., 2011]. *You et al*. [2010] also simulated the irradiance time series at 1 kHz; their data suggests that the proportion of the variance that lies within the frequency band <7 Hz increases from about 50% at 0.86 m, the shallowest depth modeled, to 92% at 2.85 m (Y. You, personal communication, 2012). Note that those data has recorded both the capillary waves and the gravity waves. In light of these facts, an instrument with a sample frequency of 7 Hz is likely sufficient to fully capture the total variance of the irradiance fluctuations induced by the gravity waves at depths >1 m.

The area of the diffuser of the radiometer is also crucial in analysis of the irradiance fluctuations at small water depths. The larger the area, the lesser the very high-frequency and high wave number irradiance fluctuations are resolved [*Dera and Stramski*, 1986]. Recent study has suggested that the irradiance fluctuations as measured below 2 m depths are likely independent of the surface area of the diffuser [*Darecki et al*., 2011]. When the sea is covered by large gravity waves, for example, the fluctuating light signals are less

sensitive to the area of the diffuser, which likely remains an appropriate spatial integrator appropriate for the interpretation of the depth evolution of the coefficient of variation in waters even shallower than 2 m.

The fall velocity of the instrument in the water column is another factor which can potentially impact the analysis of irradiance fluctuations. The instrument in our experiments fell at about 0.2–0.3 m/s; the irradiance field was sampled every 5 cm along the vertical. This strategy has been shown to be sufficient for sampling the spatial (vertical) variation of the irradiance fluctuations. We do not know yet the maximum allowed fall speed that can be adopted for representative sampling of light field fluctuations in irradiance profiles. The basic principle is that the slower the instrument falls, the more information will be resolved along the vertical.

The surface wave field includes the combined effect of waves of many different wavelengths, traveling through each other at different phase speeds, i.e., are dispersive and sometimes travelling in different directions [*Jelley*, 1989]. The differences observed in the coefficients of variation between the replicate irradiance profiles (data not shown), and between the matchups of irradiance depth profiles and fixed-position time series (Figure 12 and Table 2), to the first order, could be ascribed to the focusing effects of light by differing instantaneous sea-surface topography. But, the consistency between such data pairs is strongly suggestive of the same statistics for the dynamic air-sea boundary. The finding of consistent mean irradiance values (Figure 12c) is in concert with previous reports [*Zibordi et al*., 2009].

Our theoretical development of the dominant frequency distribution is more suggestive of dependence on environmental conditions such as the solar zenith angle and wave slopes [also see *Nikolayev et al*., 1972]. The data presented in our study represent the dynamic light field under distinctive conditions. For example, low solar zenith angles ($\sim$32°) and moderate sea states were met in the Pacific experiment, while larger solar zeniths ($\sim$48°) and relatively calmer sea states were observed in the field expedition in the Santa Barbara Channel. Since these controlling factors in our experiment varied over a very small range, the available information of the environmental dependence is limited. The two study areas discussed above differ with respect to the spectral distribution of the diffuse attenuation coefficient (Figure 5b), but show the same spectral dependence for the scattering coefficient (Figure 5c). The dominant frequencies of irradiance fluctuations are independent of optical wavelength, in accordance with previous reports [e.g., *Darecki et al*., 2011; *Gege and Pinnel*, 2011; *Gernez and Antoine*, 2009; *Stramska and Dickey*, 1998]. However, the rate of change in the variance with depth does show a spectral dependency, and decreases with increasing optical wavelength. The scattering at these four wavebands seems important in determining the vertical rate of change of the variance, since the optical scattering tends to smear out the contrast of the light field signals [*Wells*, 1973], and bring down the variance of fluctuating irradiance field. The SBC water has a mean scattering coefficient and scattering albedo much higher than the Pacific water (Figures 5c and 5d) and henceforth could lead to much more attenuated variability (Figure 11b). The spectrally decreasing sky diffuseness (Figure 5a) is partly responsible as well [*Stramski*, 1986a], but probably to a smaller degree [*Gege and Pinnel*, 2011].

6. Highlights and Summary

In this study, an effort is devoted to extracting the information on the statistics of wave-induced irradiance fluctuations from the irradiance depth profiles measured by a free-fall radiometer, and quantifying and modeling the distribution of the light field statistics along the water column at 1–40 m depths in the Pacific Ocean off Hawaii and at 1–10 m depths in the Santa Barbara Channel, respectively. This study, to our best knowledge, represents the first attempt of applying wavelet method to the statistics of the wave-induced irradiance fluctuations. Our analyses have shown that the normalized and detrended continuous irradiance depth profiles can be decomposed into fluctuations in the time-frequency domain. Two signatures of light field fluctuations, the dominant frequency and the coefficient of variation, can be further obtained from the irradiance profile decompositions. Such derived dominant frequency and coefficient of variation is comparable to those determined from fixed-position time series measurements. The modeled depth distribution of the light field statistics is not only consistent with historical reports, which were based on fixed-position measurements at a few depths, but provides the full and continuous information along the vertical. According to our results, the irradiance depth profiles may be used to describe the depth variability of the fluctuating irradiance field in terms of the

dominant frequency and the coefficient of variation, at least under similar environmental conditions (with big waves).

Notation

C_p phase speed, m s^{-1}.
E_d downwelling plane irradiance, μWcm^{-2} nm^{-1}.
$<E_d>$ mean irradiance, μWcm^{-2} nm^{-1}.
E_s downwelling plane irradiance above sea surface, μWcm^{-2} nm^{-1}.
f temporal frequency, s^{-1}.
f_p dominant frequency, s^{-1}.
F a factor relating f_p to water depth z.
F_s instrument sampling rate, Hz.
g gravitational acceleration, m s^{-2}.
H sea wave height, m.
I_n normalized irradiance residuals, dimensionless.
K_{cv} attenuation coefficient for the coefficient of variation (CV), m^{-1}.
K_d diffuse attenuation coefficient for E_d, m^{-1}.
k wave number, rad m^{-1}.
θ zenith angle, degrees or radians.
φ azimuth angle, degrees or radians.
θ_s solar zenith angle in air, degrees and radians.
w_s instrument fall speed, m s^{-1}.
ζ sea surface instantaneous elevation, m.
ζ_{xy} sea-surface slope, degrees or radians.
ω angular frequency, rad s^{-1}.
Λ sea wave length, m.
λ light wavelength, nm.
n_w refractive index of sea water.
ψ wavelet function.
S wavelet scale, s.
T Fourier period, s.
t observation time, s.
T_p dominant period, s.
W_n wavelet transform.
z water depth, m.
z_f focal depth, m.

Acknowledgments

This work was sponsored by the Office of Naval Research project "Radiance in a Dynamic Ocean" (RaDyO) under grants N00014-07-C-0139 and N00014-09-C-0084 (MRL), N00014-06-1–0372 and N00014-11-1–0168 (CJZ), and N00014-11-M-0142 (MST). MRL also acknowledges support from the Natural Sciences and Engineering Research Council of Canada. Michael Dowd is acknowledged for invaluable discussions on the data statistical analysis. Scott Freeman and Matthew Slivkoff are thanked for collection and processing of IOPs data. We appreciate the comments made by Dariusz Stramski and three anonymous reviewers which have improved the current manuscript.

References

Darecki, M., D. Stramski, and M. Sokolski (2011), Measurements of high-frequency light fluctuations induced by sea surface waves with an underwater porcupine radiometer system, *J. Geophys. Res.*, *116*, C00H09, doi:10.1029/2011JC007338.

Dera, J., and H. R. Gordon (1968), Light field fluctuations in the photic zone, *Limnol. Oceanogr.*, *13*(4), 697–699.

Dera, J., and D. Stramski (1986), Maximum effects of sunlight focusing under a wind-disturbed sea surface, *Oceanologia*, *23*, 15–42.

Dera, J., S. Sagan, and D. Stramski (1993), Focusing of sunlight by sea surface waves: New results from the Black Sea, *Oceanologia*, *34*, 13–25.

Fraser, A. B., R. E. Walker, and F. C. Jurgens (1980), Spatial and temporal correlation of underwater sunlight fluctuations in the sea, *IEEE J. Ocean Eng.*, *5*(3), 195–198.

Gege, P., and N. Pinnel (2011), Sources of variance of downwelling irradiance in water, *Appl. Opt.*, *50*(15), 2192–2203.

Gernez, P., and D. Antoine (2009), Field characterization of wave-induced underwater light field fluctuations, *J. Geophys. Res.*, *114*, C06025, doi:10.1029/2008JC005059.

Gernez, P., D. Stramski, and M. Darecki (2011), Vertical changes in the probability distribution of downward irradiance within the near-surface ocean under sunny conditions, *J. Geophys. Res.*, *116*, C00H07, doi:10.1029/2011JC007156.

Gordon, H. R. (1989), Can the Lambert-Beer law be applied to the diffuse attenuation coefficient of ocean water?, *Limnol. Oceanogr.*, *34*(8), 1389–1409.

Gordon, H. R., J. M. Smith, and O. B. Brown (1971), Spectra of underwater light-field fluctuations in the photic zone, *Bull. Mar. Sci.*, *21*(2), 466–470.

Greene, R. M., and V. A. Gerard (1990), Effects of high-frequency light fluctuations on growth and photoacclimation of the red alga Chondrus crispus, *Mar. Biol.*, *105*(2), 337–344.

Gregg, W. W., and K. L. Carder (1990), A simple spectral solar irradiance model for cloudless maritime atmospheres, *Limnol. Oceanogr.*, *35*(8), 1657–1675.
Grinsted, A., J. C. Moore, and S. Jevrejeva (2004), Application of the cross wavelet transform and wavelet coherence to geophysical time series, *Nonlinear Processes Geophys.*, *11*(5/6), 561–566.
Hieronymi, M., A. Macke, and O. Zielinski (2012), Modeling of wave-induced irradiance variability in the upper ocean mixed layer, *Ocean Sci.*, *8*(2), 103–120.
Hofmann, H., A. Lorke, and F. Peeters (2008), Temporal scales of water-level fluctuations in lakes and their ecological implications, *Hydrobiologia*, *613*(1), 85–96.
Jelley, J. V. (1989), Sea waves: Their nature, behaviour, and practical importance, *Endeavour*, *13*(4), 148–156.
Jerlov, N. G. (1976), *Marine Optics*, 231 pp., Elsevier Sci., Amsterdam.
Kirk, J. T. O. (1994), *Light and Photosynthesis in Aquatic Ecosystems*, 2nd ed., 509 pp., Cambridge Univ. Press, Cambridge, U. K.
Kumar, R. R., B. P. Kumar, A. N. V. Satyanarayana, D. B. Subrahamanyam, A. D. Rao, and S. K. Dube (2009), Parameterization of sea surface drag under varying sea state and its dependence on wave age, *Nat. Hazards*, *49*(2), 187–197.
Lewis, M. R., D. Hebert, W. G. Harrison, T. Platt, and N. S. Oakey (1986), Vertical nitrate fluxes in the oligotrophic ocean, *Science*, *234*(4778), 870–873, doi:10.1126/science.234.4778.870.
Lewis, M. R., J. Wei, R. van Dommelen, and K. J. Voss (2011), Quantitative estimation of the underwater radiance distribution, *J. Geophys. Res.*, *116*, C00H06, doi:10.1029/2011JC007275.
McFarland, W. N., and E. Loew (1983), Wave produced changes in underwater light and their relations to vision, *Environ. Biol. Fishes.*, *8*(3/4), 173–184.
McLean, J. W., and J. D. Freeman (1996), Effects of ocean waves on airborne lidar imaging, *Appl. Opt.*, *35*(18), 3261–3269.
Minnaert, M. (1954), *The Nature of Light and Color in the Open Air*, 390 pp., Dover, New York.
Morel, A., and S. Maritorena (2001), Bio-optical properties of oceanic waters: A reappraisal, *J. Geophys. Res.*, *106*(C4), 7163–7180.
Morel, A., and L. Prieur (1977), Analysis of variations in ocean color, *Limnol. Oceanogr.*, *22*(4), 709–722.
Mueller, J. L. (2003), In-water radiometric profile measurements and data analysis protocols, in *Ocean Optics Protocols for Satellite Ocean Color Sensor Validation, Revision 4*, edited by J. L. Mueller, G. S. Fargion, C. R. McClain, Natl. Aeronaut. and Space Admin., Goddard Space Flight Space Cent., Greenbelt, Md.
Mueller, J. L., G. S. Fargion, and C. R. McClain (Eds.) (2003), *Ocean Optics Protocols for Satellite Ocean Color Sensor Validation, Revision 4*, NASA, Goddard Space Flight Cent., Greenbelt, Md.
Nakamura, T., and H. Yamasaki (2008), Flicker light effects on photosynthesis of symbiotic algae in the reef-building coral Acropora digitifera (Cnidaria: Anthozoa: Scleractinia), *Pac. Sci.*, *62*(3), 341–350.
Nikolayev, V. P., and M. S. Khulapov (1976), Use of a nonstatistical model to explain the mechanism of underwater illumination fluctuation, *Izv. Atmos. Oceanic Phys.*, *12*(9), 993–997.
Nikolayev, V. P., and V. G. Yakubenko (1978), Experimental research into the spatial structure on the fluctuations of the underwater light field, *Izv. Atmos. Oceanic Phys.*, *14*(4), 301–305.
Nikolayev, V. P., O. I. Prokopov, G. V. Rozenberg, and V. I. Shevernev (1972), Statistical properties of the underwater illumination, *Izv. Atmos. Oceanic Phys.*, *8*(9), 936–944.
Preisendorfer, R. W. (1976), *Hydrologic Optics*, 218 pp., U.S. Gov. Print. Off., Honolulu, Hawaii.
Prokopov, O. I., and V. P. Nikolayev (1976), A study of underwater illumination fluctuations in the Mediterranean Sea, *Izv. Atmos. Oceanic Phys.*, *12*(5), 559–563.
Prokopov, O. I., V. P. Nikolayev, A. A. Zhil'tsov, and L. M. Nesterenko (1975), Some results of a study of light field fluctuations in the sea from the "Chernomor" underwater laboratory, *Izv. Atmos. Oceanic Phys.*, *11*(11), 1179–1183.
Quéguiner, B., and L. Legendre (1986), Phytoplankton photosynthetic adaptation to high frequency light fluctuations simulating those induced by sea surface waves, *Mar. Biol.*, 482–491.
Reda, I., and A. Andreas (2004), Solar position algorithm for solar radiation applications, *Sol. Energy*, *76*(5), 577–589.
Sathyendranath, S., and T. Platt (1988), The spectral irradiance field at the surface and in the interior of the ocean: A model for applications in oceanography and remote sensing, *J. Geophys. Res.*, *93*(C8), 9270–9280.
Schenck, H., Jr. (1957), On the focusing of sunlight by ocean waves, *J. Opt. Soc. Am.*, *47*(7), 653–657.
Schubert, H., S. Sagert, and R. M. Forster (2001), Evaluation of the different levels of variability in the underwater light field of a shallow estuary, *Helgoland Mar. Res.*, *55*, 12–22.
Siegel, D. A., and T. D. Dickey (1988), Characterization of downwelling spectral irradiance fluctuations, *Proc. SPIE*, *925*, 67–74.
Siegel, D. A., A. F. Michaels, J. C. Sorensen, M. C. O'Brien, and M. A. Hammer (1995), Seasonal variability of light availability and utilization in the Sargasso Sea, *J. Geophys. Res.*, *100*(C5), 8695–8713.
Snyder, R. L., and J. Dera (1970), Wave-induced light-field fluctuations in the sea, *J. Opt. Soc. Am.*, *60*(8), 1072–1079.
Stoll, S. (2009), Effects of light level fluctuations on the early life stages of fish in the littoral zone of lakes, PhD thesis, 168 pp., Univ. of Konstanz, Konstanz, Germany.
Stramska, M., and T. D. Dickey (1998), Short-term variability of the underwater light field in the oligotrophic ocean in response to surface waves and clouds, *Deep Sea Res. Part I*, *45*(9), 1393–1410.
Stramski, D. (1986a), The effect of daylight diffuseness on the focusing of sunlight by sea surface waves, *Oceanologia*, *24*, 11–27.
Stramski, D. (1986b), Fluctuations of solar irradiance induced by surface waves in the Baltic, *Bull. Pol. Acad. Sci. Earth*, *34*(3), 333–344.
Stramski, D., and J. Dera (1988), On the mechanism for producing flashing light under a wind-disturbed water surface, *Oceanologia*, *25*, 5–21.
Stramski, D., G. Rosenberg, and L. Legendre (1993), Photosynthetic and optical properties of the marine chlorophyte Dunaliella tertiolecta grown under fluctuating light caused by surface-wave focusing, *Mar. Biol.*, *115*(3), 363–372.
Toffoli, A., A. Babanin, M. Onorato, and T. Waseda (2010), Maximum steepness of oceanic waves: Field and laboratory experiments, *Geophys. Res. Lett.*, *37*(5), L05603,doi:10.1029/2009GL041771.
Torrence, C., and G. P. Compo (1998), A practical guide to wavelet analysis, *Bull. Am. Meteorol. Soc.*, *79*(1), 61–78.
Twardowski, M. S., X. Zhang, S. Vagle, J. M. Sullivan, S. Freeman, H. Czerski, Y. You, L. Bi, and G. Kattawar (2012), The optical volume scattering function in a surf zone inverted to derive sediment and bubble particle subpopulations, *J. Geophys. Res.*, *117*, C00H17, doi:10.1029/2011JC007347.
Voss, K. J., S. McLean, M. Lewis, C. Johnson, S. Flora, and M. Feinholz (2010), An example crossover experiment for testing new vicarious calibration techniques for satellite ocean color radioemetry, *J. Atmos. Oceanic Technol.*, *27*(10), 1747–1759.
Walker, R. E. (1994), *Marine Light Field Statistics*, 675 pp., John Wiley, New York.

Walsh, P., and L. Legendre (1983), Photosynthesis of natural phytoplankton under high frequency light fluctuations simulating those induced by sea surface waves, *Limnol. Oceanogr.*, *28*(4), 688–697.
Waters, K. J., R. C. Smith, and M. R. Lewis (1990), Avoiding ship-induced light-field perturbation in the determination of oceanic optical properties, *Oceanography*, *3*(2), 18–21.
Weber, V. (2010), Coefficient of variation of underwater irradiance fluctuations, *Radiophys. Quantum Electron.*, *53*(1), 13–27.
Wei, J., R. Van Dommelen, M. R. Lewis, S. McLean, and K. J. Voss (2012), A new instrument for measuring the high dynamic range radiance distribution in near-surface sea water, *Opt. Express*, *20*(24), 27,024–27,038.
Wells, W. H. (1973), Theory of small angle scattering, *Optics of the Sea, AGARD Lect. Ser. 61*, 3.3-1-3.3–19.
Xing, X., A. Morel, H. Claustre, D. Antoine, F. D'Ortenzio, A. Poteau, and A. Mignot (2011), Combined processing and mutual interpretation of radiometry and fluorimetry from autonomous profiling Bio-Argo floats: Chlorophyll a retrieval, *J. Geophys. Res.*, *116*, C06020, doi: 10.1029/2010JC006899.
You, Y., D. Stramski, M. Darecki, and G. W. Kattawar (2010), Modeling of wave-induced irradiance fluctuations at near-surface depths in the ocean: A comparison with measurements, *Appl. Opt.*, *49*(6), 1041–1053.
Young, I. R. (1999), *Wind Generated Ocean Waves*, 288 pp., Elsevier Sci., Oxford, U. K.
Zaneveld, J. R. V., and R. W. Spinrad (1980), An arc tangent model of irradiance in the sea, *J. Geophys. Res.*, *85*(C9), 4919–4922.
Zaneveld, J. R. V., E. Boss, and A. Barnard (2001), Influence of surface waves on measured and modeled irradiance profiles, *Appl. Opt.*, *40*(9), 1442–1449.
Zappa, C. J., M. L. Banner, H. Schultz, J. R. Gemmrich, R. P. Morison, D. A. LeBel, and T. D. Dickey (2012), An overview of sea state conditions and air-sea fluxes during RaDyO, *J. Geophys. Res.*, *117*, C00H19, doi:10.1029/2011JC007336.
Zibordi, G., D. D'Alimonte, and J. F. Berthon (2004), An evaluation of depth resolution requirements for optical profiling in coastal waters, *J. Atmos. Oceanic Technol.*, *21*, 1059–1073.
Zibordi, G., J. F. Berthon, and D. D'Alimonte (2009), An evaluation of radiometric products from fixed-depth and continuous in-water profile data from moderately complex water, *J. Atmos. Oceanic Technol.*, *26*(1), 91–106.